Research Square

Preprints are preliminary reports that have not undergone peer review.
They should not be considered conclusive, used to inform clinical practice,
or referenced by the media as validated information.

Photocatalytic Reduction for Integrated Single-vat Multimaterial 3D Printing

Andrew Boydston

aboydston@wisc.edu

University of Wisconsin, Madison https://orcid.org/0000-0001-7192-4903

Sarah Finnegan

University of Wisconsin - Madison https://orcid.org/0000-0001-6793-3380

Holden Howard

Lawrence Livermore National Laboratory

Shahryar Mooraj

Lawrence Livermore National Laboratory

Xinyu Miao

University of Wisconsin - Madison

Isabel Arias-Ponce

Lawrence Livermore National Laboratory

Drew Melchert

Lawrence Livermore National Laboratory

Kathryn Weber

University of Wisconsin - Madison

Quang Nguyen

DEVCOM Army Research Laboratory

Alex Abelson

https://orcid.org/0000-0002-5887-5278

Wonjin Choi

3Lawrence Livermore National Laboratory

Tehshik Yoon

University of Wisconsin https://orcid.org/0000-0002-3934-4973

Aldair Gongora

Lawrence Livermore National Laboratory

Maxim Shusteff

Lawrence Livermore National Laboratory https://orcid.org/0000-0001-7000-1963

Johanna Schwartz

Lawrence Livermore National Laboratory https://orcid.org/0000-0002-3709-6478

Article

Keywords:

Posted Date: November 4th, 2026

DOI: https://doi.org/10.21203/rs.3.rs-11556122/v1

License: This work is licensed under a Creative Commons Attribution 4.0 International License.
Read Full License

Additional Declarations: There is **NO** Competing Interest.

Abstract

Photocatalysis is introduced as a viable chemical scheme in vat photopolymerization additive manufacturing (AM). Specifically, we demonstrate the use of acridinium photocatalysts to facilitate reduction of silver salts toward the patterned formation of conductive silver wires. Electronic devices are typically manufactured by fabricating and assembling electrically distinct materials, a multistep approach that requires various feedstocks, energy-intensive processing, and complex workflows. Here, we introduce a chemistry-driven strategy for multimaterial AM, coined Photocatalytic Reduction for Integrated Single-vat Multimaterial 3D Printing (PRISM 3DP), in which conductive and insulating materials are synthesized directly from a single homogeneous liquid precursor. Wavelength-selective photocatalysis enables visible light to reduce metal salts and generate conductive metal pathways in situ, whereas ultraviolet light initiates acrylate polymerization to form dielectric, insulating polymer domains. Automated high-throughput photochemical screening identified resin formulations that promoted nanoparticle formation while maintaining favorable photopolymerization behavior. The resulting polymer domains exhibit an average dielectric constant of 3.9 across 8–12 GHz, comparable to dielectric materials used in commercial circuit boards. Metallic features reach conductivities up to 3×10^7 S/m, approximately half the conductivity of bulk silver, and five orders of magnitude greater than those produced without a photocatalyst under otherwise identical conditions. Using a custom platform that integrates stereolithography and digital light processing, we fabricated wires, multilayer architectures, and functional electronic circuits. This work introduces photocatalysis as a design principle for AM, demonstrating that fabrication can be coupled with spatially programmed chemical synthesis to produce complex and functional multimaterial parts from a single feedstock.

Introduction

As modern technologies increase in complexity, manufacturing strategies capable of rapidly producing electrically heterogeneous structures have become increasingly important. Despite remarkable advances in additive manufacturing (AM), electronics fabrication methods still largely rely on multistep workflows in which conductive and insulating materials are separately synthesized and processed, and then assembled through serial deposition steps.[1,2] These manufacturing processes are often slow, are energy intensive, generate significant material waste, and constrain device geometry.[3–5]

An attractive alternative is a manufacturing framework where electrically distinct materials are synthesized directly during fabrication from a single precursor material. Rather than assembling pre-existing conductors and dielectrics, chemical reactions could be patterned with light to generate distinct materials. Such a strategy would fundamentally merge chemical synthesis with manufacturing, producing conductive and insulating domains from a single feedstock through spatially controlled reactions. Vat photopolymerization (VP) stands out among AM techniques for realizing this vision because it leverages chemical transformations for the fabrication process and does so in a solution-based environment that resembles common chemical reaction setups.[6–8] This feature inspires imagination as to the limits of the chemical reactivity space that can be incorporated into VP AM, as well

as the extent to which multiple materials can be incorporated into the same part within a single fabrication process.

Chemistry-based approaches to multimaterial VP leverage strategic combinations of reactions that are specific to unique wavelengths or light intensity thresholds to yield 3D parts with distinct material domains.[9–13]At the current boundaries of materials synthesis used in VP exist straightforward photoinitiated polymerizations to yield organic polymers and networks, with resin components primarily drawn from acrylate, epoxide, alkene, and related feedstocks.[14–17] Thus, most demonstrations of multimaterial parts from VP highlight differences in mechanical properties of the constituent materials.[18,19] Work on metal salt infusion of hydrogels has yielded patterned insulating and conductive domains, however, infusion techniques are inherently restricted by the infusion particle size and hydrogel part geometry.[20–23] Additionally, the incorporation of metallic precursors in the form of dissolved salts is done in post-processing rather than during printing.

Reframing the creation of metallic domains during printing as a fundamentally bottom-up synthesis challenge invites a broader chemical space for consideration. However, combination of electrically disparate materials classes through single-resin VP remains elusive due largely to a lack of chemical means to harmonize photochemical polymerizations and photo-driven synthesis of metallic domains in a single resin system. Thermally driven synthesis of metallic species in a single resin system has yielded parts with conductive domains; however, feature resolution is inherently limited by thermal management.[24,25] Much higher resolution is achieved via two-photon polymerization, but compromises both the throughput rate as well as the ability to combine the metal and dielectric material synthesis into a single resin system.[26] More acutely, advances in chemical precision for synthesizing metallic features could unlock access to high resolution, high throughput production of multimaterial and multifunctional electronics from singular, homogeneous resin formulations.

To explore the possibility of synthesizing metallic domains during VP AM, we looked toward photo-mediated reduction of soluble metal salts. Taking inspiration from the large body of work on photoredox catalysis and related transformations of small molecules, we hypothesized that using photocatalysts in multi-wavelength VP could enable spatially resolved formation of metallic features within larger polymeric domains.[27–30] Herein, we present Photocatalytic Reduction for Integrated Single-vat Multimaterial 3D Printing (PRISM 3DP): a method for 3D printing conductive metal and insulating polymer domains from a single feedstock material, achieved by integrating a wavelength-specific photocatalytic reaction into an acrylate-based polymer system. Through sequential processing with ultraviolet digital light processing and visible light stereolithography, were able to pattern conductive features within an insulating polymer, without post-processing requirements (Figs. 1A and 1B).

Results

Reaction Design and Resin Formulation

The vision of a single resin system capable of efficiently and selectively producing both electrically conductive metallic domains and insulating polymeric networks for effective multimaterial printing required both the discovery of suitable reaction schemes for in situ metal synthesis as well as establishing wavelength specificity between the two processes for spatial control. We approached the first step of the materials down-selection with wavelength orthogonality as the threshold for progression: a reaction combination where one wavelength is used to selectively activate the photoinitiator, causing only polymerization, and a different wavelength selectively activates the photocatalyst, causing only metal salt reduction. Starting from a pool of 12 radical photoinitiators (PIs) and 30 potential photocatalysts (PCs), we identified 207 viable combinations that displayed non-overlapping regions of their UV/vis absorption spectra (Table S1). These 207 combinations then moved forward toward chemical selectivity screening experiments.

To isolate the effects of the PI and PC, these formulations included a consistent monomer, poly(ethylene glycol) diacrylate (PEGDA), and metal salt, silver trifluoroacetate (AgTFA), while varying the photosystems. Here, PEGDA and AgTFA were chosen for their prevalence in VP and high solubility in organic solutions, respectively (Table S2). Solutions were exposed to LED illumination with wavelengths that correlated to the specific PIs and PCs in each test formulation. Visual inspection was used to assess the extent of wavelength selectivity for each process (polymerization versus metal salt reduction), as well as the amount of background reactivity taking place. Qualitatively, if polymerization occurs, solidification is observed, and if metal formation occurs, a color change to brown or black is visible. Successful combinations were moved forward if background reactivity was not observed for 1 hour, and polymerization and metal salt reduction occurred to visually observable extents only when their respective wavelength of light was applied. The combination of 9-mesityl-10-methylacridinium tetrafluoroborate (Mes-Acr) as the PC and 2,2-dimethoxy-2-phenylacetophenone (DMPA) as the PI showed sufficient chemical selectivity for our down-select. (Fig. 1C). The DMPA was selectively activated with low intensity (10 mW/cm^2) 365-nm light, whereas the Mes-Acr required higher intensity (≥ 100 mW/cm^2) 405-nm light for activation. Importantly, although the Mes-Acr does absorb 365 nm light as seen in the absorption spectra (Fig. 1C), no visible metal formation is achieved at low intensity, providing material orthogonality.

Having identified a compatible PI-PC photosystem, we next sought to accelerate nanoparticle formation to enable rapid fabrication of conductive features. We therefore developed a high-throughput screening campaign to determine how monomer and crosslinker composition affect the bulk kinetics of silver nanoparticle (AgNP) formation. A custom automated platform was built by integrating a liquid handler, LED irradiation plate (420 nm, 155 mW/well), a high-throughput UV-Vis absorbance reader, and a robotic arm to formulate resins and monitor kinetic absorption data at different irradiation intervals without manual intervention (Figure S3, Method S1).

Absorbance measurements provide a semi-quantitative method to compare reaction rates between resin formulations. AgNPs exhibit localized surface plasmon resonance (LSPR) between 400 and 450 nm, with particle nucleation sizes up to approximately 100 nm, whereas AgTFA absorbs below 350 nm in the

monomers used in our study.[31] The increase in absorbance at 400 nm was used as a proxy for AgNP formation (Fig. 2A). In addition to particle nucleation and growth, AgNP aggregation can be captured using the same method, as reflected by a red shift in the LSPR spectra toward 600 nm and longer wavelengths. Monitoring increases in absorption at 600 nm is thereby a proxy for nanoparticle aggregation. In general, we hypothesize that for conductive nanoparticle network formation, a high rate of both nanoparticle formation and aggregation is required. Our initial automated screen evaluated 32 unique resin formulations, each in triplicate, with systematic variation in monomer identity and concentration. To accommodate different AgTFA solubility among monomers, we first used monomer mixtures comprised of PEGDA and 2-cyanoethyl acrylate (CNEA) in which AgTFA exhibited high solubility. In total, the initial automated screen generated 1,920 photokinetic measurements.

At low concentrations of variable monomer, which we denote by Δ (Δ:PEGDA:CNEA = 1:4:6 and 1:2:3), all formulations exhibited similar 400-nm absorbance profiles during irradiation, indicating comparable AgNP nucleation behavior. At higher rations of Δ content (Δ:PEGDA:CNEA = 2:3:1), particularly formulations without PEGDA (Δ:CNEA = 1:1), acetonitrile (MeCN), lauryl acrylate (LA), and acryloPOSS (APOSS) produced less AgNP formation. In contrast, triethylolpropane triacrylate (TMPTA), hydroxypropryl acrylate (HPA) and tertrahydrofuranyl acrylate (THFA) modestly increased the rate of AgNP formation. Changes in 600-nm absorbance, an indicator of AgNP aggregation, generally followed the trends observed in AgNP formation, suggesting that formulations promoting rapid nanoparticle generation also tended to promote aggregation. However, MeCN, THFA, and HPA exhibited disproportionately large increases in 600-nm absorbance relative to 400-nm. These results suggest that these formulations preferentially promote particle growth or aggregation after nucleation, rather than solely increasing the rate of AgNP generation.

Collectively, this first screening campaign demonstrated that AgNP formation is chemically modular, with several formulations supporting favorable nanoparticle formation and aggregation. Exploring trends in the results, they seem to suggest that monomer oxidation potential, Ag(I) coordination, and viscosity are potentially key variables governing these processes. Because conductive nanoparticle networks are expected to require both rapid AgNP formation and efficient aggregation, formulations that showed both strong 400-nm and 600-nm responses are of greatest interest. With this in mind, our screenings led us to target lower viscosity formulations based upon 600-nm monitoring. By this criterion, the top three performing variable monomers are MeCN, THFA, and HPA. Additionally, for nanoparticle formation, our top three candidates based upon the 1:1 Δ:CNEA results were TMPTA, PEGMEA, and HPA. As HPA is ranked high in both analyses, we selected hydroxy acrylates and methacrylates for continued investigation. For further discussion of chemical trends and results from the first screening campaign, please see Discussion S1.

A second automated screen focused on the hydroxy acrylates and methacrylates, based upon the promising performance of HPA in the initial automated screen, potentially reflecting its low viscosity and the relative ease of the alcohol oxidation (Fig. 2B). A small amount of diacrylate crosslinker was included in the formulation to facilitate curing (monomer:crosslinker = 3:1, v:v). The second screening yielded

AgNP formation rates comparable to those observed in the first screen, with faster nanoparticle aggregation. While in general the four formulations of the second automated screen performed within experimental error of each other, suggesting all could be used for future printing efforts, 3:1 hydroxyethylmethacrylate:triethyleneglycol dimethacrylate (HEMA:TEGDMA v:v) was chosen as the final formulation, as it showed the highest average rates of nanoparticle formation and aggregation. A proposed mechanism for the photocatalytic synthesis of AgNP can be seen in Fig. 2C. However, further mechanistic studies are needed to understand the various contributing factors and elucidate the primary mechanistic pathway.

Finally, to ensure that the cured polymer would be sufficiently insulating as a dielectric material upon printing, the dielectric properties were measured over a frequency sweep from 8 to 12 GHz. After curing the complete resin formulation with 365-nm light, we measured a relative permittivity of approximately 3.87, which is comparable to that of insulating materials used in commercially manufactured circuit boards (Figs. 2D and 2E).[32–35]

Fabrication of Conductive Features

Having chosen a precursor composition allowing for both photopolymerization and photoreduction through high-throughput screening, we identified the manufacturing irradiation requirements needed to create highly conductive and insulating features from our feedstock resin. The two reactions imposed substantially different light source demands. Photoinitiated radical polymerizations are photon efficient: one absorbed photon can initiate a chain polymerization involving hundreds or thousands of propagation steps, enabling curing under modest irradiation (on the order of 10 mW/cm^2). In contrast, an idealized photoreduction process produces a single redox event per photon and therefore requires greater photon flux. Additionally, the photocatalytic reaction has a lower quantum yield than the radical photoinitiation with DMPA (approximately 0.04 compared to 0.42, respectively, Figure S4).[36] We therefore anticipated that commercially available DLP projectors would not be able to provide sufficient irradiance for the photoreduction reaction to create conductive pathways within timescales of 10s of seconds relevant to AM.

Toward this end we built a system with a variable intensity 405-nm scanned laser that could irradiate either through a resin vat or directly onto a build plate (Figure S4). This enables rapid screening experiments to test irradiation parameters with a variety of resin formulations, and the ability to make complex geometric patterns. The laser-writing platform produced visible nanoparticle pathways within the resin across a large exposure window (0.13–1.70 kJ/cm^2). Increasing laser exposure also visibly increased the amount of nanoparticle formation, eventually producing a defect-free wire with a strong metallic luster (Figs. 3A and 3B). To examine the mechanism of wire formation, we fabricated wires across a range of exposures (0.08–1.70 kJ/cm^2) and characterized them by scanning electron microscopy (SEM).

At 0.08 kJ/cm^2, before a wire is optically visible, a sparse layer of aggregated nanoparticles ranging from 10 to 200 nm in diameter forms, visible by SEM (Fig. 3Ci). While aggregated, the individual particle boundaries are clearly visible. At 0.34 kJ/cm^2 exposure, an optically visible wire forms, and the density of particles significantly increases, although void space remains (Fig. 3Cii). Increased vertical depth of particles is also visible, with smaller particles (defined here as approximately 10–100 nm diameter) appearing below larger aggregates (approximately 200 nm – 1 μm diameter). Irregular, non-spherical silver aggregate features, with no clear internal particle boundaries, are also present, suggesting some onset of sintering. These sintered structures extended several micrometers in length, however, there is no clear percolation pathway, further indicated by a resistance measurement greater than the multimeter maximum of 500 MΩ. At 0.85 kJ/cm^2 exposure, sintered nanoparticles cover nearly the entire substrate and form clear percolation pathways despite some small void space, further supported by conductivity values of 1.3×10^5 S/m (Fig. 3Ciii). Finally, at 1.70 kJ/cm^2 exposure, silver nanoparticles completely cover the substrate, producing conductivity values of 1.1×10^7 S/m (Fig. 3Cvi). SEM reveals at least three discernible layers of nanoparticles, with the layers closest to the substrate showing few particle boundaries and many percolation pathways, and smaller nanoparticles sparsely covering the surface. By programming the laser coordinates, we were able to produce custom silver wire patterns across a range of exposures (Fig. 3D).

When measuring conductivity across a range of irradiation conditions, an analogous resin without photocatalyst was an important control, as it is well documented that silver nanoparticles can be synthesized by thermal decomposition of silver salts at high temperature (≥ 300 ˚C, decomposition temperature varies by salt, Figure S5). However, thermal processing couples feature resolution to heat transport rather than to the spatial and temporal control of light. A predominantly photochemical process is therefore preferable for retaining the high resolution associated with VP.

Measuring the conductivity of wires made with the control resin across the same range of total light exposure showed that the PC-containing resin produced conductive wires at nearly half the exposure required for the control resin to produce conductive wires (0.51 and 0.85 kJ/cm^2, respectively, Fig. 3E). At 0.85 kJ/cm^2 exposure, the PC-containing resin produced wires with roughly 5 orders of magnitude greater conductivity than the control resin (1.3×10^5 S/m and 1.7 S/m, respectively). To achieve conductivity on the order of 10^5 S/m the control resin required nearly double the energy input as the PC-containing resin. Above 1.70 kJ/cm^2 exposure, the resins produced wires with similar conductivities with or without photocatalyst. These results indicate that the photocatalytic pathway dominates wire formation over an exposure range of approximately 0.8–1.6 kJ/cm^2.

In addition to varying total light exposure while keeping laser intensity constant (3.4 kW/cm^2), it is important to compare the impact of laser intensity on final wire conductivity. Keeping total light exposure constant at 1.27 kJ/cm^2, to target the photocatalytic regime, at every laser intensity tested, the control resin produced wires with lower conductivity than with PC present (Fig. 3F). The optimum laser intensity for producing highly conductive wires in the PC-containing resin was 2.54 kW/cm^2. At this intensity, with

the PC present, wires with 3×10^7 S/m conductivity, approximately half the conductivity of bulk silver, can be fabricated. [37] We again see nearly 5 orders of magnitude difference in conductivity between wires produced with the photocatalytic resin and the control system without PC. Above 2.54 kW/cm^2 laser intensity, conductivity decreases by up to an order of magnitude, even with the PC included.

Figure 3. (**A**) Diagram of wire formation process showing stepwise nanoparticle formation to ultimate aggregation, left to right. (**B**) Optical microscopy images of wires fabricated with increasing amounts of 405-nm exposure (all scale bars = 100 μm). (**C**) Scanning electron microscopy images of wires fabricated with a 3.4 kW/cm^2 laser and (**i**) 1laser pass; total exposure of 0.08 kJ/cm^2 (**ii**) 4 laser passes; total exposure of 0.34 kJ/cm^2 (**iii**) 10 laser passes; total exposure of 0.85 kJ/cm^2, and (**iv**) 20 laser passes; total exposure of 1.70 kJ/cm^2 (all scale bars = 2 μm). (**D**) Silver periodic table symbol made of printed silver wires fabricated with 3.40 kW/cm^2 intensity laser and 0.84 kJ/cm^2 total exposure (scale bar = 1 mm), inset: SEM of wire intersection (scale bar = 1 μm). (**E**) Plot of wire conductivity as a function of total exposure at constant 3.40 kW/cm^2 laser intensity (error bars are present for all data points and represent the coefficient of variation of 3 replicate wires).[37] (**F**) Plot of wire conductivity as a function of laser intensity at constant 1.27 kJ/cm^2 exposure (error bars are present for all data points and represent the coefficient of variation of 3 replicate wires).[37]

Multimaterial Circuit Manufacturing

Having chosen the multimaterial resin formulation and photo-processing parameters for dielectric and conductive performance we next fabricated multicomponent circuits to demonstrate the capabilities of the platform. We first evaluated the electrical performance of the printed wires by patterning circuit connections on a glass substrate and reflow-soldering a push button controller, LED, and resistor to the printed connections (Fig. 4Ai). Notably, the silver wires produced in this demonstration were synthesized using the complete multicomponent resin by applying only the 405-nm laser for metal salt reduction. Conductive silver ink was used to make contact between the voltage source and the printed wire. The LED remained off when the switch was open, and illuminated when the switch was pushed closed, confirming reliable fabrication of a closed circuit (Figs. 4Aii and 4Aiii).

We next fabricated a multilayer circuit combining both the radical-mediated dielectric and the photocatalytically generated conductive wires into the same design (Fig. 4B). Using a 365-nm projection, a 500 μm layer of resin was cured onto a glass substrate. We then used 405-nm laser patterning onto the polymer surface to drive photoreduction and form silver wires in desired locations. Repeating these steps produced a multilayer circuit structure containing dielectric domains with embedded conductive features. We connected LEDs and voltage sources using conductive silver ink to complete the device (Fig. 4C). Applying a voltage to either circuit selectively illuminated the desired LED. Notably, successful functioning of the LED of the bottom layer circuit indicated that conductivity of printed wires was

preserved under complete dielectric encapsulation, and that this insulation enables discrete control of both circuits without crosstalk.

This demonstration established that multilayer circuitry can be fabricated from a single resin formulation by varying only the spatial application of different colors of light. DLP exposure at 365 nm produces an insulating polymer matrix, whereas 405-nm laser exposure generates the conductive pathways for electronics design. The approach therefore provides a simple route to future generation of integrated three-dimensional circuits without changing feedstock material between fabrication steps.

Discussion

This work establishes a novel strategy for multiwavelength 2D and 3D printing of electronic circuits from a single multimaterial resin. This is enabled by spatially programmed wavelength control, dictating either in situ generation of silver nanoparticles via photocatalysis (405 nm) or photopolymerization of dielectrically insulating polymer (365 nm) from a single homogenous photoresin. The resulting material domains exhibit electrically distinct behavior, and the demonstration of multilayer circuits highlights the potential of this chemistry to produce embedded conductive architectures without material exchange. Notably, the ability to synthesize metallic features in situ during printing represents a conceptual departure from conventional approaches to multimaterial AM.

Further improvements in nanoparticle growth, coalescence, and percolation could increase conductivity and expand the range of device architectures accessible through this approach. A more detailed understanding of the photoreduction mechanism, including the roles of electron donors, metal coordination, and resin viscosity, may also enable improved reaction efficiency and greater control over feature formation. Increasing photocatalyst efficiency will be important for extending the method to additional material systems and applications.

More broadly, these results establish photocatalysis as a new design principle for multimaterial AM. Rather than merely patterning pre-existing materials, this framework centers the concept of synthesizing functional materials during AM processes. Extending this framework to other photocatalytic transformations, including the synthesis of semiconductors, magnetic materials, or preceramics, could substantially expand the functional landscape of VP and bridge the gap between chemical synthesis and manufacturing.

Methods

Materials 2-Hydroxyethyl methacrylate (HEMA), 2-hydroxyethyl acrylate, poly(ethylene glycol) diacrylate (average M_n 500), acetonitrile (MeCN), 2,2-dimethoxy-2-phenylacetophenone (DMPA), 9-mesityl-10-methylacridinium tetrafluoroborate (acridinium), poly(ethylene glycol) methylether acrylate (PEGMEA), hydroxypropyl acrylate (HPA), 2-hydroxyethyl acrylate (HEA), poly(ethylene glycol) diacrylate (average Mn 575, PEGDA), trimethylpropane triacrylate (TMPTA), tetrahydrofuranyl acrylate (THFA), and

trimethylolpropane ethoxylate triacrylate (TMPETA) were purchased from Sigma Aldrich. Silver trifluoroacetate (AgTFA) was purchased from Ambeed. Acryloxypropyl POSS (APOSS) Cage Mixture was purchased from Hybrid Plastics. Triethylene glycol dimethacrylate (TEGDMA) was purchased from Tokyo Chemical Industry. Silver conductive ink (liquid S-020) was purchased from Alfa Aesar. $Bi_{57}Sn_{42}Ag_1$ solder flux was purchased from ChipQuik.

Resin Formulation The optimized resin was formulated by adding 3:1 (v:v) HEMA:TEGDMA, 3.2 M AgTFA, and 0.3 mM acridinium to a scintillation vial. The vial was sonicated until all AgTFA had dissolved. 0.5 weight % DMPA was added to the solution, and the vial was manually shaken until DMPA was dissolved. The vial was wrapped in aluminum foil to prevent ambient light exposure and stored at 0 ˚C prior to use. Resin was returned to room temperature before printing.

Binary Polymerization and Reduction Screening Resin was added to a 1 cm × 1.5 cm × 0.3 cm Teflon mold. The resin was irradiated using a Kessil lamp (approximately 300 mW/cm^2, wavelength corresponding to the specific photocatalyst or photoinitiator) affixed 1 cm above the top of the mold.

HTP Reduction Screening High-throughput resin screening was performed using a custom automation platform. The platform integrated an Opentrons OT-2 liquid handler, a Byonoy Absorbance 96 plate reader, a Lumidox II 96-Well 420-nm LED Array, and a UFactory robot arm, with custom Python code. Detailed information on the design of the automation platform can be found in Figure S3 and Method S1.

Laser Printing An Oxxius LBX-405-HPE fiber-coupled 405 nm laser with variable intensity up to 5.37 kW/cm^2, was focused onto the bottom surface of a 2 inch × 3 inch glass slide mounted on Thorlabs MCM301 XY stage. Liquid resin was contained on the glass slide with a 1 mm adhesive silicone gasket. The XY stage moved at 3 mm/s and was controlled with a custom Python script. A detailed description of the laser printing apparatus is included in Figure S4.

Insulating Layer Fabrication Liquid resin was injected between an FEP lined glass slide and an untreated glass slide separated with 500 µm spacers. The stack was physically masked and irradiated through the FEP lined glass slide surface with a Prizmatix UHP-F-365 LED at 100% intensity (approximately 50 mW), approximately 10 cm away from the slide surface, for 60 seconds. After curing the two glass slides were separated and uncured resin was washed with acetonitrile.

Resistivity Measurements 4 dots of conductive silver paste we applied across the length of the wires then the glass slide was placed on a 150 ˚C for 15 minutes. A Keithley 2400 SourceMeter was used on the 4-wire sense mode to measure the resistance across the wire. The distance between the inner two silver paste points was measured with a Keyence optical microscope. The height profile of the wire was measured with a Zygo Profilometer. A custom Python script was used to extract the average cross-sectional area of the wire from the glass substrate. Resistivity was calculated using $\rho = \frac{R \bullet A}{L}$, where R is resistance, A is cross-sectional area, and L is length.

Circuit Fabrication

Wires on Glass Substrate Printed wires were cleaned with acetonitrile. A syringe of $Bi_{57}Sn_{42}Ag_1$ solder paste was affixed with a Nordson EFD Smooth Flow Tapered Tip (200 μm). An LED, resistor, and push button were affixed to their corresponding connections, and a drop of solder paste was deposited to each of their leads. The circuit was placed in a GF-B-HT re-flow oven from Novastar and heated from room temperature to 170 ˚C in 10 minutes, then held at 170 ˚C for 1 minute (oven under air at 1 atm). The circuit was removed from the oven and cooled to room temperature. Silver paste was applied to the lead wires and heated at 150 ˚C for 15 minutes. The circuit was cooled to room temperature, and the power supply probes were applied to the silver paste pads.

Multimaterial Circuit Conductive silver paste was applied to the circuit connections. An LED was affixed to the corresponding connections. A heat gun at approximately 150 ˚C was applied to the connections for approximately 60 s to cure the conductive silver paste. The circuit. The circuit was cooled to room temperature, and the power supply probes were applied to the silver paste pads.

Instrumentation

Dielectric Measurement Resin was added to a 25 mm × 12 mm × 3 mm Teflon mold and cured with 370 nm light and placed in a rectangular waveguide. The complex permittivity (ε) and permeability (μ) of the material were characterized using a transmission-reflection-line waveguide method with a vector network analyzer. Two-port scattering parameters were measured and converted to complex permittivity using the Nicolson-Ross-Weir retrieval method.[38] To reduce sensitivity to uncertainties in the sample position, a reference-plane invariant formulation was implemented.[39]

Rheological Data was collected on a TA Instruments Discovery HR-1 Hybrid Rheometer with a 12 mm parallel plate geometry. Reported viscosity values are the average across a 60 s measurement at a constant shear rate of 200 s^{-1} with 1 s step times at room temperature.

Scanning Electron Microscopy was performed on a ThermoFisher Apreo 2 SEM at 5.00 kV.

Optical Microscopy images were collected on a Keyence VHX digital microscope.

Profilometry measurements were made on a Zygo Zegage Pro HR profilometer. A custom python script was used to mask the area surrounding the wire and extract the average cross-sectional area of the wire.

Declarations

Acknowledgments

The authors acknowledge funding support from the DARPA AMME program. A.J.B. acknowledges partial financial support from the Yamamoto Family, the Office of the Vice Chancellor for Research and Graduate Education at the University of Wisconsin-Madison with funding from the Wisconsin Alumni Research Foundation. This work was performed under the auspices of the United States Department of

Energy by Lawrence Livermore National Laboratory under Contract DE-AC52-07NA27344, LLNL-JRNL-2022634. Distribution Statement "A" (Approved for Public Release, Distribution Unlimited). The authors would like to acknowledge Dr. Julianna Mouat and Prof. Dan Weix for their helpful discussions.

Author Contributions Statement

Conceptualization: S.G.F.; K.M.W.; T.P.Y.; M.S.; J.J.S.; A.J.B. Data Curation: S.G.F. Funding Acquisition: S.G.F.; A.A.; M.S.; J.J.S.; A.J.B. Investigation: S.G.F.; H.J.H.; X.M.; S.M.; I.F.A.; K.M.W.; Q.M.N.; A.A.; W.C. Methodology: S.G.F.; H.J.H.; A.E.G.; J.J.S.; Software: S.G.F.; H.J.H.; S.M.; W.C.; D.S.M.; A.E.G. Supervision: T.P.Y.; A.E.G.; M.S.; J.J.S.; A.J.B. Visualization: S.G.F. Writing – original draft: S.G.F. Writing – reviewing & editing: S.G.F.; M.S.; J.J.S.; A.J.B.

Competing Interests Statement

Authors declare that they have no competing interests.

Data Availability

The data supporting this study is available within the Article and Supplementary Information. Data files in other formats are available from the corresponding author upon request.

References

1. Bell NS, Sarobol P et al (2016) Additive manufacturing of hybrid circuits. Annu Rev Mater Res
2. Persad J, Rocke S (2022) Multi-material 3D printed electronic assemblies: A review. Results Eng 16:100730
3. Annankra JA, Sefa-Boateng Y (2025) Evaluating the environmental impact of electronics production and the advancement in sustainable manufacturing processes. World J Adv Res Rev 28(1):126–134
4. Rao CH, Avinash K, Varaprasad BKSVL, Goel SA (2022) Review on Printed Electronics with Digital 3D Printing: Fabrication Techniques, Materials, Challenges and Future Opportunities. J Electron Mater 51:2747–2765
5. Khan Y, Thielens A, Muin S, Ting J, Baumbauer C, Arias AC (2020) A New Frontier of Printed Electronics: Flexible Hybrid Electronics. Adv Mater 32:1905279
6. Bagheri A, Jin J (2019) Photopolymerization in 3D Printing. ACS Appl Polym Mater 1(4):593–611
7. Zhang F, Zhu L, Li Z, Wang S, Shi J, Tang W, Li N, Yang J (2021) The recent development of vat photopolymerization: A review. Addit Manuf 48(B):102423
8. Pagac M, Hajnys J, Ma Q, Jancar L, Hansa J, Stefek P, Masicek J (2021) A review of vat photopolymerization technology: Materials, applications, challenges, and future trends of 3D printing. Polymers 13(4):598
9. Chin KCH, Ovsepyan G, Boydston AJ (2024) Multi-color dual wavelength vat photopolymerization 3D printing via spatially controlled acidity. Nat Commun 15:3867

10. Gholami F, Yue L, Li M, Jain A, Mahmood A, Fratarcangeli M, Ramprasad H, Qi HJ (2024) Fast and Efficient Fabrication of Functional Electronic Devices through Grayscale Digital Light Processing 3D Printing. Adv Mater 36:2408774
11. Forte CT, Montgomery SM, Yue L, Hamel CM, Qi HJ (2023) Grayscale Digital Light Processing Gradient Printing for Stress Concentration Reduction and Material Toughness Enhancement. J Appl Mech 90(7):071003
12. Kiker MT, Recker EA, Uddin A, Page ZA (2024) Simultaneous Color- and Dose-Controlled Thiol-Ene Resins for Multimodulus 3D Printing with Programmable Interfacial Gradients. Adv Mater 36(40), e2409811
13. Montgomery SM, Yue L, Song Y, Nomura T, Sun X, Tanaka M, Qi HJ (2023) Locally patterned anisotropy using grayscale vat photopolymerization. Addit Manuf 73:103687
14. Diaco NS, Thrasher CJ, Hughes MM, Zhou KA, Durso MN, Yap S, Macfarlane RJ, Hart AJ (2025) Dual-Wavelength Vat Photopolymerization With Dissolvable, Recyclable Support Structures. Adv Mater Technol 10(17):e00650
15. Howard HJ, Alameda BM, De Beer MP, Mettry-Yassa M, Schwartz JJ, Terrel-Perez D (2025) Hybrid Additive and Subtractive Manufacturing of Dual-Wavelength Photopolymer Thermosets. *Adv. Mater. Technol.* e00997
16. Arias Ponce I, Moran B, Hawker CJ, Shusteff M, Huang S (2025) Dual-Wavelength Simultaneous Patterning of Degradable Thermoset Supports for One-Pot Embedded 3D Printing. ACS Cent Sci 11(6):967–974
17. Mason KS, Kim J, Recker EA, Nymick JM, Shi M, Stolpen FA, Ju J, Page ZA (2025) Multicolor Digital Light Processing 3D Printing Enables Dissolvable Supports for Freestanding and Non-Assembly Structures. ACS Cent Sci 11(6):975–982
18. Schwartz JJ, Boydston AJ (2019) Multimaterial actinic spatial control 3D and 4D printing. Nat Commun 10:791
19. Kim JW, Allen MJ, Recker EA, Stevens LM, Cater HL, Uddin A, Gao A, Eckstrom W, Arrowood AJ, Sanoja GE, Cullinan MA, Freeman BD, Page ZA (2025) Hybrid epoxy–acrylate resins for wavelength-selective multimaterial 3D printing. Nat Mater 24:1116–1125
20. Ji Y, Su E, Yee DW (2025) Volumetric Additive Manufacturing of Composites via Hydrogel Infusion. ACS Mater Lett 7(8):2850–2857
21. Saccone MA, Gallivan RA, Narita K, Yee DW, Greer (2022) J.R. Additive manufacturing of micro-architected metals via hydrogel infusion. *Nature* 612, 685–690
22. Ji Y, Hong Y, Bhandari DR, Yee DW (2026) Hydrogel-Based Vat Photopolymerization of Ceramics and Metals with Low Shrinkages via Repeated Infusion Precipitation. Adv Mater 38(8):e04951
23. Finnegan SG, Kinsey AM, Boydston AJ (2025) Selective infusion of spatially controlled domains via vat photopolymerization 3D-printing for chemically diverse multimaterial parts. Nat Commun 16:11258

24. Xiao J, Zhang D, Guo Q, Yang J (2021) 3D Co-Printing of 3D Electronics with a Dual Light Source Technology. Adv Mater Technol 6:2100039
25. Kim Y, Alam M, Lee C, Lee BJ, Baik S (2026) Silver ion resin with large UV penetration depth for highly conductive digital light processing 3D printing. Adv Compos Hybrid Mater 9(61)
26. Saha SK, Au B, Oakdale JS (2019) High-Speed Direct Laser Writing of Silver Nanostructures via Two-Photon Reduction. Adv Eng Mater 21(9):1900583
27. Nicewicz DA, Nguyen TM (2014) Recent Applications of Organic Dyes as Photoredox Catalysts in Organic Synthesis. ACS Catal 4(1):355–360
28. Yoon T, Ischay M, Du J (2010) Visible light photocatalysis as a greener approach to photochemical synthesis. Nat Chem 2:527–532
29. Schultz DM, Yoon TP (2014) Solar Synthesis: Prospects in Visible Light Photocatalysis. Science 343:1239176
30. Xuan J, Xiao W (2012) Visible-Light Photoredox Catalysis. Angew Chem Int Ed 51:6828–6838
31. Agnihotri S, Mukherji S, Mukherji S (2014) Size-controlled silver nanoparticles synthesized over the range 5-100 nm using the same protocol and their antibacterial efficacy. RSC Adv 4:3974
32. Mumby SJ, Yuan J (1989) Dielectric Properties of FR-4 Laminates as a Function of Thickness and the Electrical Frequency of the Measurement. J Electron Mater 18(2)
33. Bei R, Qian C, Zhang Y, Chi Z, Liu S, Chen X, Xu J, Aldred MP (2017) Intrinsic low dielectric constant polyimides: relationship between molecular structure and dielectric properties. J Mater Chem C 5(48):12807–12815
34. Gonon P, Sylvestre A (2002) Dielectric properties of fluorocarbon thin films deposited by radio frequency sputtering of polytetrafluoroethylene. J Appl Phys 92(8):4584–4589
35. Fuscaldo W, Maita F, Maiolo L, Beccherelli R, Zografopoulos DC (2022) Broadband Dielectric Characterization of High-Permittivity Rogers Substrates via Terahertz Time-Domain Spectroscopy in Reflection Mode. Appl Sci 12:8259
36. Marien YW, Van Steenberge PHM, Kockler KB, Barner-Kowollik C, Reyniers M, Marin GB (2017) D'hooge, D.R. Estimating the photodissociation quantum yield from PLP-SEC peak heights. Polym Chem 8(20):3124–3128
37. Haynes WM (2016) CRC Handbook of Chemistry and Physics, 97th edn. CRC, Boca Raton, FL
38. Nicolson AM, Ross GF (1968) Measurement of the intrinsic properties of materials by time domain techniques. IEEE Trans Instrum Meas IM–19:395–402
39. Chalapat K, Sarvala K, Li J, Paraoanu GS (2009) Wideband reference-plane invariant method for measuring electromagnetic parameters of materials. IEEE Tran Microw Theory Tech 7(9):2257–2267

Figures

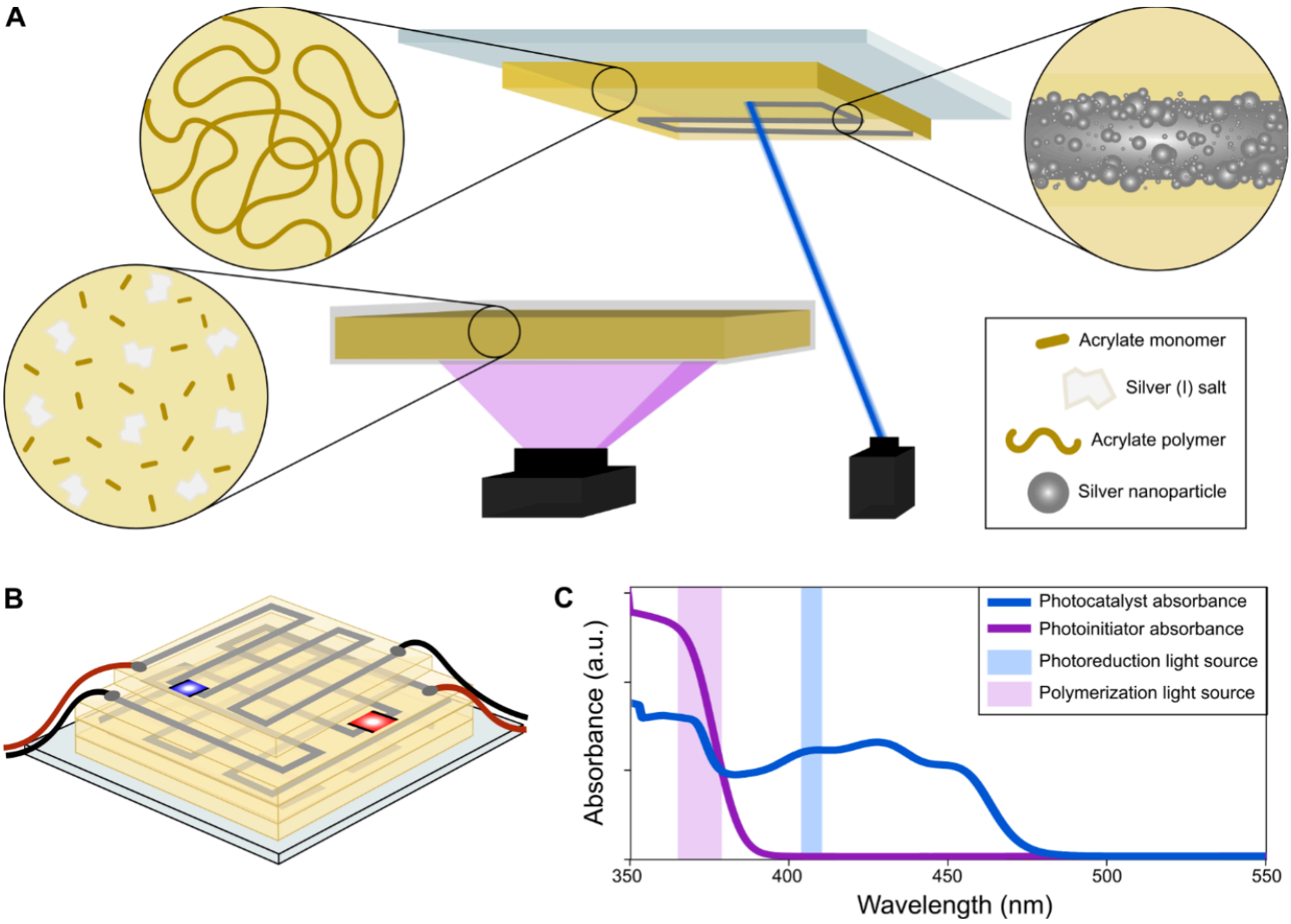


Figure 1

(A) Diagram of multiwavelength printing with 365-nm projector curing acrylate resin and 405-nm laser reducing silver salt to silver nanoparticles. (B) Diagram of representative multi-layer printed part with added circuitry components. (C) Absorbance spectra of the photocatalyst for metal salt reduction and the photoinitiator for acrylate polymerization with the wavelength range of the corresponding activating light source overlayed (arbitrarily scaled y-axis units for visualization).

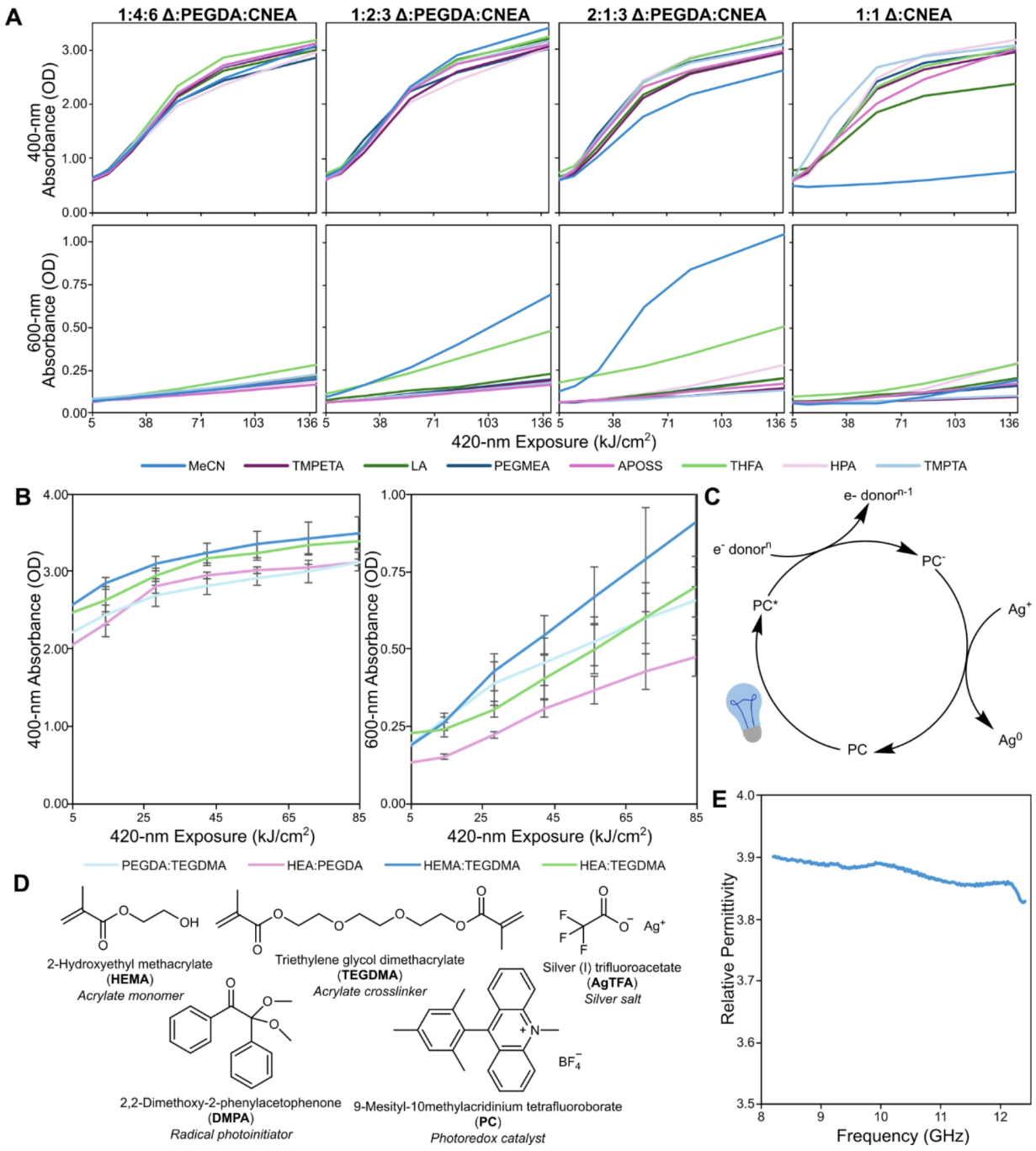


Figure 2

(A) Automated high-throughput monomer screen photokinetic data indicative of silver nanoparticle formation (400 nm) and aggregation (600 nm) as a function of irradiation. Δ Indicates the ratio of the monomer variable. Data points represent averages of 3 replicate formulations. (MeCN = acetonitrile, TMPETA = trimethylolpropane ethoxylate triacrylate, LA = lauryl acrylate, PEGMEA = poly(ethylene glycol) methylether acrylate, APOSS = acryloPOSS, THFA = tetrahydrofuranyl acrylate, HPA = hydroxypropyl

acrylate, TMPTA = trimethylolproprane triacrylate). (B) Automated high-throughput photokinetic screen of monomer:crosslinker formulations in 3:1 ratios (v:v). Data points represent averages of 3 replicate formulations. Error bars represent the standard deviation of the 3 replicate formulations. (PEGDA = poly(ethylene glycol) diacrylate, TEGDMA = triethylene glycol dimethacrylate, HEA = 2-hydroxyethylacrylate, HEMA = hydroxyethyl methacrylate). (C) Proposed mechanism for photocatalytic reduction of silver salt. (D) Final resin formulation components. (E) Dielectric measurement frequency sweep of 3:1 HEMA:TEGDMA (v:v) resin formulation after curing with 365-nm light.

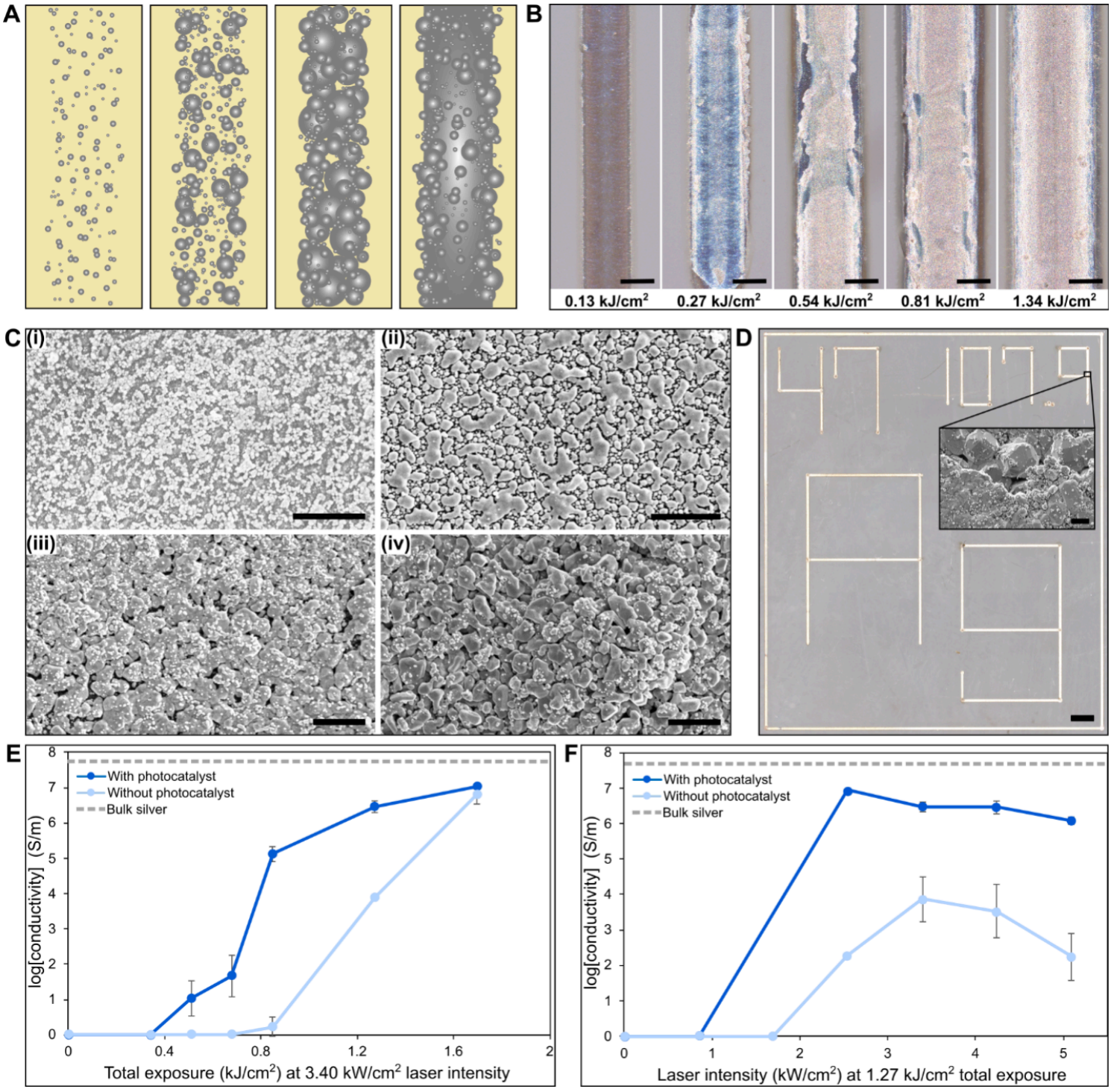


Figure 3

(**A**) Diagram of wire formation process showing stepwise nanoparticle formation to ultimate aggregation, left to right. (**B**) Optical microscopy images of wires fabricated with increasing amounts of 405-nm exposure (all scale bars = 100 μm). (**C**) Scanning electron microscopy images of wires fabricated with a 3.4 kW/cm^2 laser and (**i**) 1laser pass; total exposure of 0.08 kJ/cm^2 (**ii**) 4 laser passes; total exposure of 0.34 kJ/cm^2 (**iii**) 10 laser passes; total exposure of 0.85 kJ/cm^2, and (**iv**) 20 laser passes; total exposure of 1.70 kJ/cm^2 (all scale bars = 2 μm). (**D**) Silver periodic table symbol made of printed silver wires fabricated with 3.40 kW/cm^2 intensity laser and 0.84 kJ/cm^2 total exposure (scale bar = 1 mm), inset: SEM of wire intersection (scale bar = 1 μm). (**E**) Plot of wire conductivity as a function of total exposure at constant 3.40 kW/cm^2 laser intensity (error bars are present for all data points and represent the coefficient of variation of 3 replicate wires).[37] (**F**) Plot of wire conductivity as a function of laser intensity at constant 1.27 kJ/cm^2 exposure (error bars are present for all data points and represent the coefficient of variation of 3 replicate wires).[37]

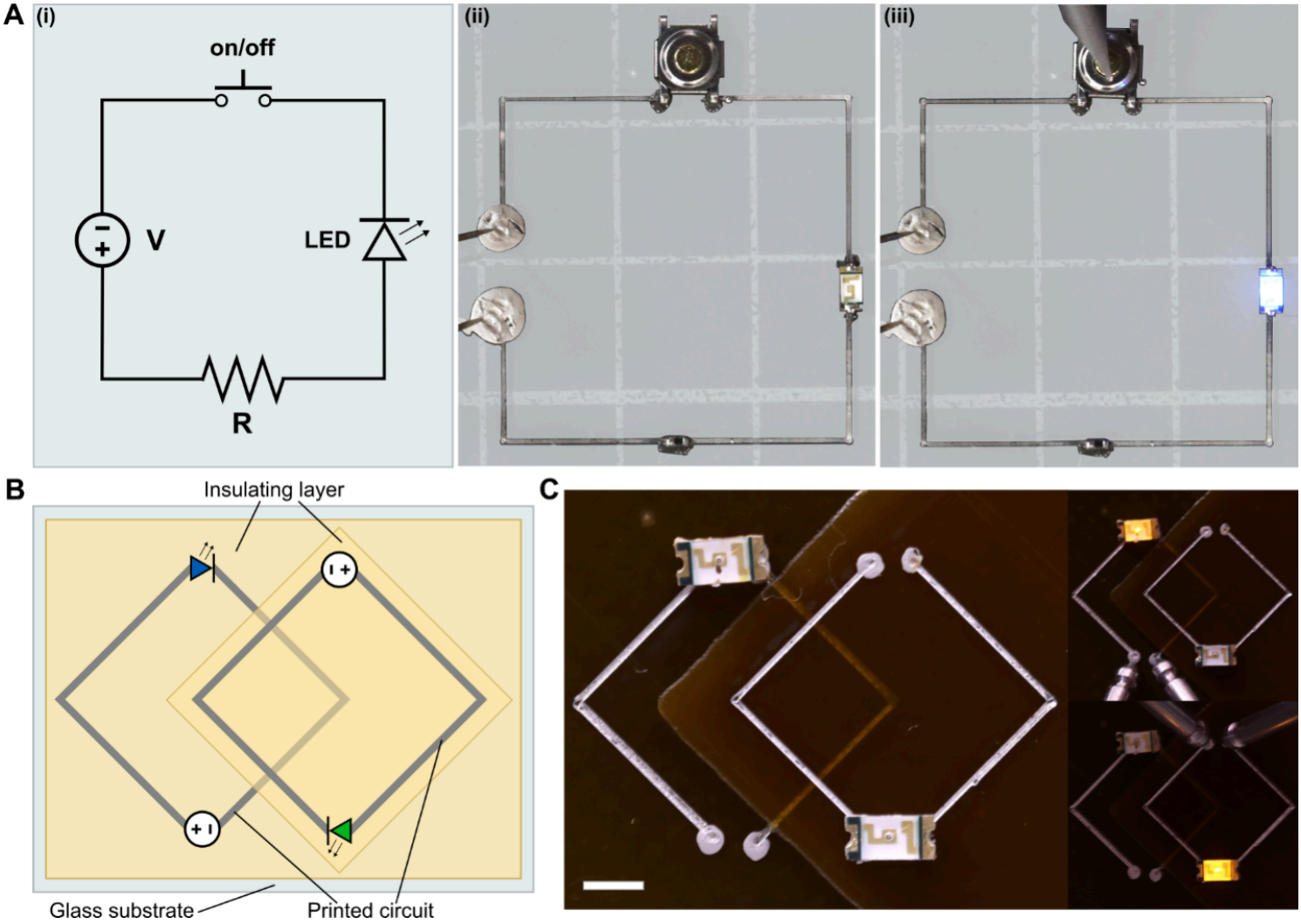


Figure 4

(**A**) Wire circuit showing the (**i**) circuit design, (**ii**) photograph of printed circuit with the push button in the off position and the LED unilluminated, and (**iii**) photograph of printed circuit with the push button in the

on position and the LED illuminated. (**B**) Diagram of multi-layer circuit. (**C**) Photograph of multilayer circuit with both LEDs unilluminated (left, scale bar = 2 mm), bottom-layer circuit LED illuminated (right top), and top-layer circuit illuminated (right bottom).

Supplementary Files

This is a list of supplementary files associated with this preprint. Click to download.

- PRISMSINatureComm.docx